

Effect of a magnetic field in photodetachment microscopy

W. Chaibi, R.J. Peláez, C. Blondel^a, C. Drag, and C. Delsart

Laboratoire Aimé-Cotton (CNRS), Université Paris-Sud, Bât. 505, 91405 Orsay Cedex, France

Received 23 December 2009 / Received in final form 19 February 2010

Published online 13 April 2010 – © EDP Sciences, Società Italiana di Fisica, Springer-Verlag 2010

Abstract. The effect of an external static magnetic field of arbitrary orientation with respect to the electric field, on the electron interference ring patterns observed by the photodetachment microscope is studied both experimentally and theoretically. The design of the interaction chamber has been modified to superimpose a controlled uniform magnetic field on the whole volume accessible to the interfering electron. Contrary to a previous study in weaker fields, where the overall dimension of the interferogram was not modified, the effect of the magnetic field here encompasses a regime of magnetic refocusing. A quantitative analysis is carried out using a closed-orbit perturbative calculation of the interference phase at the centre of the ring pattern. The essential result of this work is still the invariance of the extreme interference phase whatever the direction and magnitude of the applied magnetic field, up to values 100 times larger than in the previous experimental study. This property can be applied to revise former electron affinity measurements. Partly due to the previously unsuspected robustness of the electron interferograms vs. magnetic fields, partly thanks to the 2006 CODATA revision of the energy conversion factors, one can update the values of the electron affinities of ^{16}O , ^{28}Si and ^{32}S to 1.4611134(9), 1.3895210(7) and 2.0771040(6) eV respectively.

1 Introduction

Photodetachment microscopy [1,2] has been used since 1996 for showing that electron interferences can be produced in a uniform electric field [3] and for the best-ever electron affinity measurements on atoms [4] and molecules [5]. This technique uses the near-threshold photodetachment of negative ions by a monochromatic laser field, which provides an almost point-like source of low-energy electrons with fixed kinetic energy and the emission of a spherical electron wave. An external uniform electric field \mathbf{E} plays the role of a ‘wave-folder’ for this electron wave. In such a field, the electron undergoes constant acceleration, as in free fall, so every point within reach on the detector is hit by two parabolic trajectories, along which the electron travels simultaneously to finally interfere with itself. The variations of the phase difference between the two trajectories give rise to an interference pattern, or interferogram, which, due to the cylindrical symmetry of the problem, takes the form of concentric rings. The radius of this ring pattern is just the classical maximum off-axis distance that can be reached by the projectile, i.e. at first order the product of the initial ejection velocity V_0 by the time-of-flight T to the detector [1,2]. The electron interferogram, hence the fringe interval, are made large enough to be observable by setting the detector at a macroscopic distance z_0 , typically 0.5 m, from the detachment region. From the beginning of the experiments with the photodetachment microscope, a particular effort

was made to avoid possible effects of the Earth magnetic field by shielding the whole uniform-field region with an efficient double layer of μ -metal [2].

However the question remained of the effect an external static magnetic field \mathbf{B} could have on the electron interferograms observed by the photodetachment microscope. Two distinct aspects can be considered. On the one hand the classical trajectories are modified by the Lorentz force due to the magnetic field, which leads to a shift of the interferograms on the detector. On the other hand, there is an additional phase difference produced between every pair of unperturbed trajectories, proportional to the flux of the magnetic field between them.

Recently, but for magnetic fields \mathbf{B} still small enough to produce the same linear shift on all trajectories, we provided experimental and theoretical evidence that the interferograms only undergo a global shift, in other words that the fringe shift is just the same as the trajectory shift [6]. However, though both effects were maximised by choosing a magnetic field perpendicular to the trajectories, the case tells nothing of what happens at higher B values, namely when the cyclotron frequency $\Omega = eB/m$ (with m the electron mass and e the absolute value of the electron charge) is no longer negligible compared to T^{-1} .

The aim of the present study is to enter such a higher-field regime, in which the deflection by the Lorentz force ceases to be proportional to B , and can no longer be assumed identical for all trajectories. Theoretical calculations in this case have been made only for exactly parallel uniform electric and magnetic fields, either when

^a e-mail: christophe.blondel@u-psud.fr

the photodetachment is of the s -wave type (isotropic, as obtained e.g. for threshold photodetachment from S^- ions) [7,8] or of the p -wave type (e.g. for H^- ions) [9]. This tells but little of what may happen experimentally, for one can never guarantee perfect parallelism of the fields, and even a small transverse component of the magnetic field can obviously have dramatic effects on the magnetic flux.

Even though they do not provide the same insight as photodetachment microscopy, it is worth mentioning that numerous experimental and theoretical studies have been devoted to photodetachment *spectroscopy* in the presence of a uniform electric field [10] or in the presence of a uniform magnetic field [11,12]. In both cases, the near-threshold photodetachment cross-section, which is a smooth function of the energy, exhibits a field-induced modulation. For an external electric field, the origin of this modulation is the same phenomenon that produces the interference pattern brought to observation by photodetachment microscopy. In short words, the effect of the electric field is to reflect the half of the outgoing electron wave that escaped “uphill” in the electrostatic potential, and make it interfere with the “downhill”-emitted half-wave. In the presence of an external magnetic field, the oscillation reflects the quantization by Landau levels for the transverse motion of the photoelectron in the detachment continuum.

Photodetachment in the presence of both an electric and a magnetic field remains an area little studied experimentally, even though many theoretical studies were devoted to this domain for parallel fields [7,8,13–15], for crossed fields [13–16], and for arbitrary oriented fields [17–19]. Recently, near-threshold s -wave photodetachment spectra of S^- in parallel electric and magnetic fields have been measured and interpreted [20], and the dynamics of mono-energetic electrons in the presence of uniform, perpendicular magnetic and electric fields has been analyzed theoretically [21].

We report here some theoretical and experimental results on S^- photodetachment interferograms obtained when a uniform magnetic field is superimposed to the uniform electric field used in the photodetachment microscope, in a regime where the cyclotron frequency becomes of the same order of magnitude as T^{-1} . This is still a weak-field regime in the sense that the cyclotron frequency Ω yet remains small when compared to the inverse of the maximum time-of-flight *difference* ΔT between interfering trajectories. In the higher field domain, in which $\Omega > \Delta T^{-1}$, theory actually predicts more complicated interference patterns [7,8], the experimental investigation of which is left to further studies.

This paper is organized as follows. Section 2 describes the arrangement for the present experiment. Section 3.1 presents the observed behaviour of the ring patterns with different values of an applied longitudinal magnetic field, together with an interpretation based on the properties of the classical motion of a charged particle in constant fields and some simulations. Section 3.2 shows the robustness of the ring patterns and of the measured electron affinities in a transversal magnetic field. Such a property is applied in

Section 4 to give a revised value of the electron affinity of ^{32}S , and to update the corresponding values for ^{16}O and ^{28}Si . The conclusion discusses the essential results of the present experiment and suggests future directions of the work. In the appendix we present the details of our closed-orbit perturbative calculation of the interference phase.

2 Experimental set-up

Photodetachment microscopy in a magnetic field is performed on a beam of sulfur negative ions $^{32}S^-$. The general scheme of the experiment is presented in Figure 1. The S^- ion beam, the laser excitation, the interaction chamber and the electron detection have been described previously [4], and only the specific modifications of the set-up will be pointed out in this paper. The laser wavelength (≈ 596.9 nm) is tuned to provide an excitation just above the $^2P_{3/2} \rightarrow ^3P_2$ fine-structure component of the detachment threshold, i.e. the ground-level to ground-level transition the energy of which defines the electron affinity of sulfur [22]. For electron affinity measurements, the laser passes twice, forth and back, on the ion beam, which makes it possible to eliminate the unknown residual Doppler shift [23,24]. This is the reason for the production of double electron spots, as in the experimental examples presented below.

In the previous design of the interaction zone, magnetic shielding was achieved inside the vacuum chamber by means of a double concentric layer of μ -metal so as to minimize the residual magnetic field [2]. In contradistinction to this former situation, we now want to actively control the value of the three Cartesian components of the magnetic field \mathbf{B} , namely B_z for the component parallel to the vertical electric field, B_y for the horizontal one parallel to the mean ion beam velocity \mathbf{V}_{ion} and B_x for the other horizontal one. For this purpose, a new combination of magnetic shielding and coils was developed, the scheme of which is presented in Figure 2.

Inside the vacuum chamber, only the outer μ -metal cylinder remains. The inner one is replaced by a solenoid that consists of a one-layer coil of 1 mm wire wound on a stainless steel cylinder whose dimensions are given in Figure 2. This provides a magnetic field \mathbf{B} parallel to the electric field \mathbf{E} that can be assumed uniform all over the interaction zone, with a conversion factor of about 1.2 mT per A. Outside the vacuum chamber, we have built a system of two crossed pairs of rectangular coils whose dimensions given in Figure 2 are designed to ensure the best possible homogeneity to the magnetic field components perpendicular to the electric field. Each coil consists of 40 turns of a copper wire. With a 1 A maximum current, due to the partial shielding by the μ -metal cylinder, we obtain an effective transverse magnetic field of about $1 \mu T$ inside the interaction chamber, which can be measured by the transverse shift of the pattern due to the Lorentz force. With a flight distance $z_0 = 0.514$ m, the spot shift on the detector is $4.3 \text{ mm}/\mu T$.

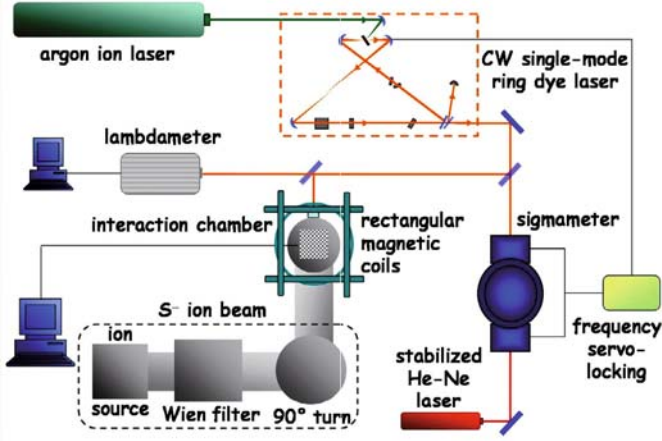


Fig. 1. (Color online) General scheme of the experimental setup. The arrangement of the magnetic coils around and inside the interaction chamber is shown in a more detailed way in Figure 2.

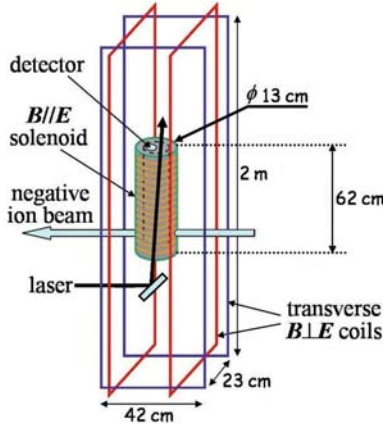


Fig. 2. (Color online) New design of the interaction chamber: a longitudinal magnetic field ($B//E$) is created by an internal solenoid on the inner face of a μ -metal shield; a transverse magnetic field ($B\perp E$) is created by two external crossed pairs of Helmholtz-type rectangular coils.

3 Experimental results with classical and quantum interpretations

3.1 Spot shifts and refocusing

The response of the electron spot to a longitudinal magnetic field ($B//E$) is illustrated by Figure 3. Double-pass spots have been recorded in the same frame for different values of the magnetic field at fixed values of the electric field and laser wavelength.

The position of the spot on the detector is determined by the motion of the electron in the directions perpendicular to the electric and magnetic fields and the position at which this cyclotron motion is interrupted after a finite time of flight T . Because the photoelectron initial kinetic energy ε is very small compared to the final kinetic energy eEz_0 , time T , within a very good approximation, can be considered as identical for all trajectories,

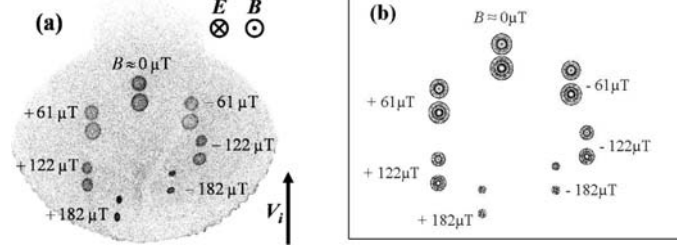


Fig. 3. General behaviour of the double-pass interferograms for increasing values of the longitudinal applied magnetic field B_z in an electric field $E = 291$ V/m (laser wavelength $\lambda = 596.885$ nm, distance to the detector $z_0 = 0.514$ m, ion beam velocity $V_{ion} = 42.4$ km/s). The diameter of the $B = 0\mu\text{T}$ lower spot (≈ 1.5 mm) gives the spatial scale of the recordings. (a) Experimental test with positive and negative values of the magnetic field up to $|B| = 182\mu\text{T}$ (solenoid current: ± 150 mA). (b) Trajectory simulations in these experimental conditions, with the additional assumption of a permanent transverse magnetic field of $0.112\mu\text{T}$ oriented at a 50.7° angle with respect to the ion velocity and a 0.29° misalignment of the variable ‘vertical’ field with respect to the electric field, with a projection in the detector plane at a 26° angle with respect to the ion velocity. This is the best combination of misalignment and residual field that reproduce the asymmetry observed in (a).

explicitly $T \cong \sqrt{\frac{2mz_0}{eE}}$. When T happens to be an integer multiple of the cyclotron period $t_c = \frac{2\pi}{\Omega} = 2\pi \frac{m}{eB}$, or equivalently when the magnetic field B is an integer multiple of $B_1 = \pi \sqrt{\frac{2mE}{ez_0}}$, the cyclotron motion brings all trajectories together to the ‘origin’, i.e. to the vertical projection of the photodetachment point onto the detection plane. This re-focusing effect concerns both the mean electron trajectory that starts with the ion velocity V_{ion} and ends at the centre of the electron spot and the whole set of trajectories corresponding to the photodetached electron wave. At the field $B_z = B_1$, with $B_1 \approx 252\mu\text{T}$ in the experimental example, the electron spots would simultaneously come back to their respective ‘origins’ and get re-focused to their minimum size.

The projection of the average electron trajectory on the detector plane is always an arc of a circle with a fixed arc length $V_{ion}T$ and a radius equal to the cyclotron radius $R_c = \frac{V_{ion}}{\Omega} = \frac{mV_{ion}}{eB}$. The spots in Figure 3 are thus expected at distances R from their ‘origin’ given by

$$R = V_{ion}T \frac{|\sin \tau|}{|\tau|} \quad (1)$$

where $\tau = \Omega T/2$ is the angular deviation of the position of the spot from the direction of the ion velocity. This is the equation of a cochleoid. The symmetry axis of this cochleoid is the projection of the ion beam velocity. Even though V_{ion} does not necessarily lie along the Oy axis of the detector, most of the asymmetry observed in Figure 3 actually comes from the sensitiveness of the cochleoid to transverse magnetic fields, either due to a residue of the Earth magnetic field or to a misalignment of the variable longitudinal magnetic field with respect to

the electric field. Fitting a calculated cochleoid to the experimental series of positions of the electron spot appears as a very sensitive way of measuring this misalignment. Figure 3 shows that a constant transverse magnetic field typically one thousandth of the longitudinal one and a misalignment of the longitudinal magnetic field of the order of 5 mrad with respect to the electric field are enough to produce a conspicuous asymmetry of the spot distribution, when the longitudinal field is varied from $-B_1$ to $+B_1$. In addition, inhomogeneities of the electromagnetic field, not taken into account in the calculation, may explain the experimental deviations of some experimental spots from a perfectly circular shape.

In the ideal case of perfectly parallel \mathbf{E} and \mathbf{B} fields, due to the linearity of the final electron position as a function of its initial velocity, the radius ρ of the electron spot, which is met by the furthest-reaching horizontally-emitted trajectories, is given by a formula quite similar to (1):

$$\rho = V_0 T \frac{|\sin \tau|}{|\tau|} = V_0 T \frac{|\sin(\frac{\Omega T}{2})|}{|\frac{\Omega T}{2}|}. \quad (2)$$

The only difference between (1) and (2) is that the latter is dimensioned, as for the initial velocity, not by the ion velocity but by the relative velocity \mathbf{V}_0 of the electron with respect to the ion's rest frame. Explicitly $V_0 = \sqrt{2\varepsilon/m}$, with ε the initial kinetic energy of the photoelectron. The factor $V_0 T = 2\sqrt{\frac{\varepsilon z_0}{eE}} = \rho_{max}$ is the radius of the spot in the pure electric field case, i.e. the maximum distance an electron can fall off the average trajectory for trajectories starting with a completely transverse initial velocity.

As a consequence of these laws, the experimental variations of the distance R of the spot centre from the origin (described by (1)) and of the spot radius ρ (described by (2)) can be plotted as functions of the same variable, which can be the current intensity in the solenoid. Figure 4 actually shows that both radii vary essentially according to the same $|\sin\tau|/|\tau|$ law. The asymmetry of the R variations is just the consequence, in this diagram, of the fact that the asymmetry of the cochleoid illustrated by Figure 3 does not only result from an asymmetry of the angular position of the spots with respect to the central axis of the figure, but contains some asymmetry of the distance to the origin too. On the other hand the spot radius ρ results from the transformation of a complete 3D sphere of initial velocities into a 2D set of final positions. The peculiarities that appear when one considers the transformation of one particular velocity are thus smoothed out. This is why the radius ρ of the spot appears far less sensitive to the existence of a residual constant field and to misalignment than the displacement R , as demonstrated by the better symmetry of the spot radius curve in Figure 4. One can check that the second maximum of the spot radius, arising around $B \approx 1.5B_1$, is about one fifth of ρ_{max} .

In three dimensions, the electron motion is a combination of the cyclotron motion just described and of a uniform acceleration in the direction of the electric field. The radial electronic distribution expands and contracts at the cyclotron angular frequency, i.e. with a period $t_c = 2\pi/\Omega$.

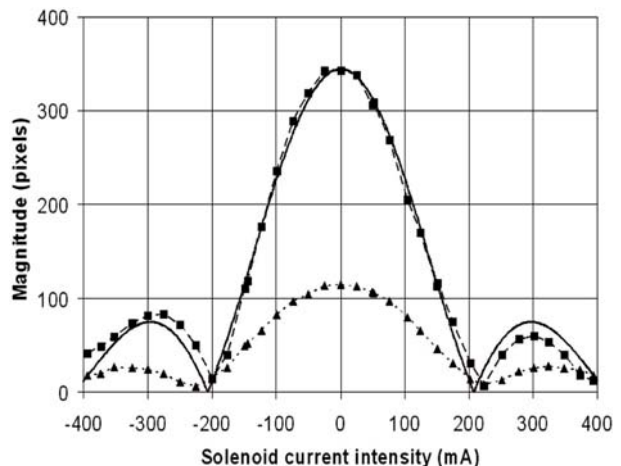


Fig. 4. Experimental plot, in detector pixels, of the distance R of the spot centre to the origin (full square ■) and of the spot average radius ρ (full triangle ▲), as functions of the current intensity in the solenoid (in mA). The measurements were carried out on one-pass interferograms (electric field $E = 291$ V/m, laser wavelength $\lambda = 596.806$ nm, distance to the detector $z_0 = 0.514$ m, ion beam velocity $V_{ion} = 42.4$ km/s). Measurements of R are compared to a calculation (full curve $-$) of formula (1) with a solenoid conversion factor 1.216 mT/A and a maximum distance $R_0 = 344$ pixels.

Figure 5 shows how the electron trajectories develop in three dimensions in the absence of any drift effect (i.e. supposing a zero ion beam velocity). Refocusing occurs as soon as t_c gets smaller than the time-of-flight T , at focal zones that get closer and closer to one another as the magnetic field increases. More explicitly, these focal zones are centred at vertical coordinates $z_k = k^2 z_1$, ($k = 1, 2, \dots$), where $z_1 = \frac{eE}{2m} t_c^2 = 2\pi^2 \frac{mE}{eB^2}$ is the z coordinate of the first focal region.

Focal regions, which are diffraction-limited anyway, are semi-classically tiny diamond-shaped caustic-limited volumes, inside which four trajectories (instead of two) intersect at every point [25]. The dimensions of these focal regions depend on z_0 , z_1 and the maximum distance the electron can go against the electric force before being reflected: $a = \varepsilon/eE$. With initial kinetic energies of typically $100 \mu\text{eV}$ and fields of a few 10^2 V m $^{-1}$, a is a fraction of a μm . Observing that $a \ll z_0$ is another way of telling that, in the experiment, the initial electron kinetic energy is always much smaller than eEz_0 .

For the particular value $B = B_1$, the radius of the focal zone, or minimum radius ρ_{min} , obtained either by the semiclassical interference of four trajectories or by the exact quantum solution, is approximately equal to a [25]. A simple relation exists between ρ_{min} and the radius ρ_{max} in the pure electric field case, namely:

$$\rho_{max} \approx 2\sqrt{\rho_{min} z_0} \quad (3)$$

with the typical parameter values of our photodetachment microscope, $\varepsilon \approx 100 \mu\text{eV}$, so $V_0 \approx 6$ km/s, $z_0 \approx 0.514$ m, $E \approx 200$ V/m, we get $T \approx 0.17 \mu\text{s}$, $\rho_{max} \approx 1$ mm and $\rho_{min} \approx 0.5 \mu\text{m}$. Refocusing takes place as soon as

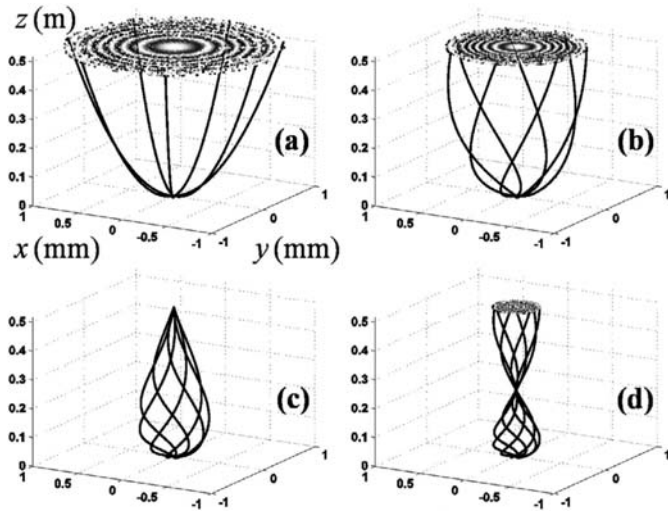


Fig. 5. 3D trajectories of electrons ejected at the origin in a uniform electric field $\mathbf{E} = -E\mathbf{u}_z$ ($E = 223$ V/m) with an initial transverse velocity $V_0 = 6.6$ km/s ($\varepsilon = 100$ m $^{-1}$), for different values of the longitudinal magnetic field $\mathbf{B} = B\mathbf{u}_z$: (a) $B = 0$, (b) $B = 0.11$ mT, (c) $B = 0.22$ mT, (d) $B = 0.33$ mT. The focalizations observed in (c) and (d) are respectively obtained for $z = z_1 \approx 0.52$ m and 0.23 m (see text for notations and explanations). In each case the interferograms resulting from the interference between trajectories with different orientations of the initial electron velocity are represented in the detector plane located at $z = z_0 = 0.52$ m.

the magnetic field absolute value exceeds $B_1 \approx 200$ μ T. Unfortunately, as rightly noticed in [7,8], the order of magnitude of ρ_{min} is such that the four-wave interference pattern expected in the focal regions are much too small to be resolved by the presently used detectors, the spatial resolution of which remains of the order of 100 μ m.

3.2 Invariance of the interferogram and robustness of the measured electron affinities

The response of the electron interferogram to a transverse magnetic field ($\mathbf{B} \perp \mathbf{E}$), in a $\Omega \ll T^{-1}$, regime was the first experimental test of the influence of a magnetic field in photodetachment microscopy. A typical example was shown in Figure 3 of reference [6], with field values from 0 to 1.3 μ T. One could observe a macroscopic translation of the electron spot perpendicular to the magnetic field, due to the Lorentz force, without any noticeable change either of the ring structure or of the value of the interference phase at the centre of the pattern. Moreover, measurements of the electron affinity by the double pass technique [4] did not reveal any significant shift within usual uncertainties. These results agree with the theoretical expectations derived from the perturbative calculation developed in the appendix. The smallness of the perturbation by a weak transverse magnetic field is now daily used in our photodetachment microscopy experiment to adjust the spot position on the detector.

The theory of the electron flux distribution in a photodetachment microscope submitted to parallel electric and magnetic fields is simple enough to give rise to analytic semi-classical expressions as well as a full quantum solution in the form of a series for the Green function [7,8]. The framework for the semi-classical description is the set of electron trajectories that start from the negative ion with a given kinetic energy ε , hence the same initial velocity V_0 in all angular directions. As already sketched by Figure 5, the resulting spiralling trajectories trace out caustic surfaces, which act as boundaries between regions with different numbers of interfering paths. The parameter introduced by Bracher et al. [7,8] as the ratio of the initial magnetic and electric forces acting on the electron

$$\eta = V_0 B / E \quad (4)$$

is just half the ratio of the cyclotron frequency Ω to the inverse of the maximum difference ΔT of the time-of-flights between interfering trajectories, which we already used to characterize our experimental regime as a weak-field one. In rough numbers, our experimental conditions correspond to $B \sim 10^{-4}$ T and $\Delta T \sim 10^{-10}$ s at most, so parameter η remains of the order of 10^{-4} – 10^{-3} , which is actually a small quantity. From an intuitive point of view, with $\eta \ll 1$ i.e. $\Omega \Delta T \ll 1$, it is conceivable that no significant magnetic phase difference has time to develop between the trajectories. This does not contradict the fact that classical effects of the magnetic field like deflection and refocusing have plenty of time to develop during time-of-flight T , which is a few 10^{-7} s, as described above.

As seen in Section 3.1, existence of a non-negligible ion velocity V_{ion} determines the distribution of the electron spots on the detector, as a function of the B_z magnetic field. In the pure photodetachment microscopy configuration (i.e. with no magnetic field), it was demonstrated, both with a relativistic argument and by an explicit calculation [26], that emission of the photoelectron wave from such a moving frame does not introduce any change in the interferograms. Presence of a magnetic field orthogonal to the ion velocity of course produces a transverse motional electric field $\mathbf{E}_{mot} = \mathbf{V}_{ion} \wedge \mathbf{B}$ (which, for the classical part of the problem, is just another way to describe the Lorentz force). At a velocity $V_{ion} = 42.4$ km/s, even with the highest parallel magnetic field $B = 0.15$ mT used in the present work for interferometry, the motional electric field is only 6 V/m, which only produces a $+0.2\%$ (second order) variation of the modulus of the electric field. The E -field correction due to the transverse magnetic field is a first order correction, but the maximum transverse magnetic field that we use, 1.5 μ T, is 100 times smaller than the longitudinal one, hence a still smaller correction. Corrections to the phase due to the motional electric field are thus expected to remain negligible. The relative variation of the magnetic field due to the symmetrical $\mathbf{B}_{mot} = -\frac{1}{c^2} \mathbf{V}_{ion} \wedge \mathbf{E}$ term is even smaller (of the order of 10^{-6}).

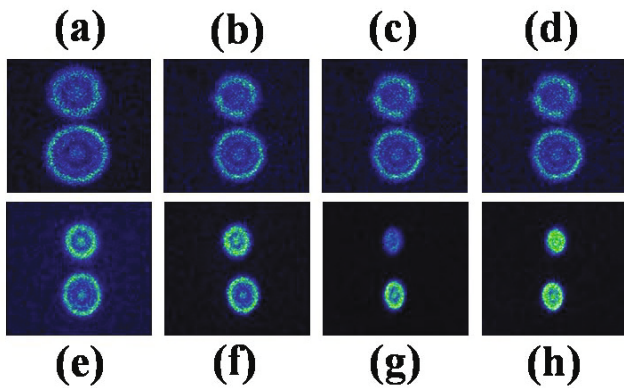


Fig. 6. (Color online) Experimental recordings of the double-pass interferograms for increasing values of the longitudinal applied magnetic field B in an electric field $E = 291$ V/m (laser wavelength $\lambda = 596.89122(4)$ nm). (a) $B = 2.1$ μT ; (b) 30.6 μT ; (c) 60.9 μT ; (d) 90.7 μT ; (e) 122.1 μT ; (f) 152.0 μT ; (g) 183.6 μT ; (h) 183.6 μT with an additional perpendicular magnetic field of about 1 μT . The 3.3 mm height of each double spot image gives the length scale.

Applying a magnetic field will also produce some spectral broadening of the detachment threshold, due to some Zeeman effect both in the negative ion and in the final neutral atom [20,27]. The order of magnitude of the resulting spectral half-width is $\hbar\Omega$. For a magnetic field of 0.15 mT, this is about 1.4×10^{-6} m^{-1} , which is, for the present experiment, one more negligible effect.

Figure 6 is a magnification of the double spots of Figure 3 that shows that the interference rings and the whole interferogram vary homothetically with the parallel magnetic field according to formula (2), and that they are insensitive to an additional perpendicular magnetic field, in agreement with previous results [6]. These experimental results completely agree with the explicit calculation of the higher-order phase variations made in the appendix, which shows that, with the experimental magnetic fields of the present work, phase corrections are expected to remain completely negligible.

This magnetic field invariance can be confirmed quantitatively by a numerical fitting of the spots, so as to extract a measurement of the electron affinity of sulfur from every pair. Since this fitting essentially consists in matching the phase of the interferogram with the analytical formula, any influence of the magnetic field on the phase would produce a deviation of the measured electron affinity from its zero-field value. Figure 7 shows, on the contrary, that the electron affinity measurements carried out in the presence of a magnetic field exhibit no significant deviation outside the limits currently set by zero-field eA measurements.

Figure 8 displays the same measurements as a function of the applied magnetic field, which would make any longitudinal magnetic field dependence conspicuous, but puts all transverse-field data together, close to the origin. The slope uncertainty that accompanies the linear regression of the measured affinity as a function of the applied magnetic field makes complete invariance close to being the most probable result.

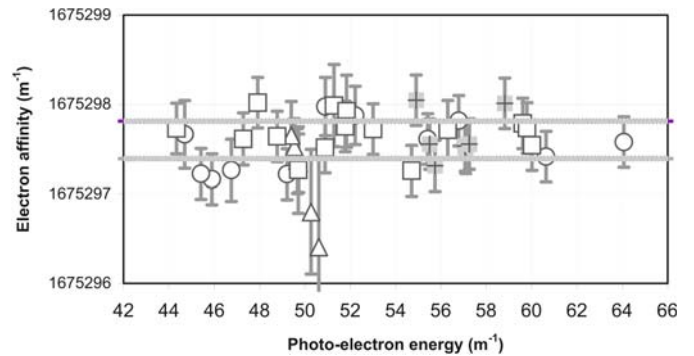


Fig. 7. Electron affinity measurements carried out in different magnetic field configuration, as a function of the mean photo-electron energy, in an electric field of either 291 or 255 V/m. Circles \circ are for a zero applied magnetic field, crosses $+$ for a transversely applied magnetic field between -0.7 and 1.3 μT , squares \square with a longitudinal magnetic field of either 60 or 90 μT , triangles Δ for exactly the same excitation wavelength and a longitudinal magnetic field up to 150 μT . For this case, magnetic field values no longer small with respect to $B_1 \approx 252$ μT produce significant refocusing that strongly reduces the accuracy of the fitting procedure, hence the exotic points with larger error bars. The two horizontal lines show the $\pm 2\sigma$ limits of our current knowledge of the electron affinity of sulfur [22].

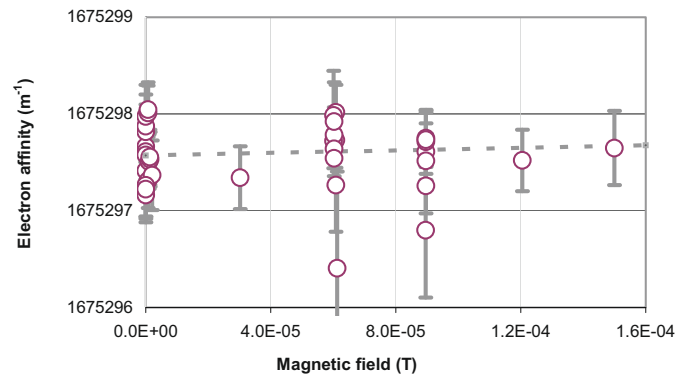


Fig. 8. Electron affinity measurements (same data as Fig. 7) as a function of the applied magnetic field B . Vector \mathbf{B} can be either parallel or perpendicular to the electric field, but the deviation by the Lorentz force is such that transverse fields cannot be greater than one and a half μT . Correspondingly all transverse field data coalesce near the origin. The measured trend is a 0.7 ± 1.3 m^{-1}/mT slope, which confirms numerically the absence of any net effect of the magnetic field on the interferograms.

4 Revision of some electron affinities

The visual aspect of photodetachment interferograms and the quantitative electron affinity measurements carried out in magnetic fields up to a few 10^{-4} T show the invariance of the phase of these interferograms and electron affinity measurements, within experimental uncertainties, as a function of the applied magnetic field. There is no magnetic field shift of the apparent electron affinity such as the one we erroneously modelled when we ‘revisited’ the

electron affinity of oxygen, silicon and sulfur in 2005 [4]. The mistake was that in the moving reference frame that would cancel the transverse magnetic field, the velocity of the ions can become such that one must not only use the relativistic expression for the transformation of the electromagnetic field, but a relativistic expression for the action integrals too. Within the limits of the present accuracy of electron affinity measurements, the possible ‘magnetic’ error that we had estimated can be reduced to zero, which can lead to one more improvement of the electron affinities of O, Si and S.

The electron affinity of oxygen however, as measured by the photodetachment microscope, was not so sensitive to the (wrong) correction formula. So the measured electron affinity remains $1178467.6(7) \text{ m}^{-1}$. The only improvement concerns the eV value of ${}^eA(^{16}\text{O})$, because the 2006 CODATA revision of the physical constants [28] comprised a threefold improvement of the m^{-1} to eV conversion factor, which makes it possible to write now ${}^eA(^{16}\text{O}) = 1.4611134(9) \text{ eV}$.

Revision of the silicon data produces a significant improvement of the electron affinity of Si, which now appears to be $1120724.4(6) \text{ m}^{-1}$, i.e. ${}^eA(^{28}\text{Si}) = 1.3895210(7) \text{ eV}$ (that is, in eV, a nearly twofold accuracy improvement).

The electron affinity of sulfur was the subject of more and more accurate electron affinity measurements since 2005 [22,29], which have produced an up-to-date value of the electron affinity of $1675297.53(41) \text{ m}^{-1}$, i.e. ${}^eA(^{32}\text{S}) = 2.0771040(6) \text{ eV}$. Revision of the 2005 data does not add to this accuracy; ${}^eA(^{32}\text{S})$ remains the most accurately known of all electron affinities.

5 Conclusion

Photodetachment microscopy was carried out in the presence of magnetic fields two orders of magnitude larger than those used in a preliminary study. Invariance of the interval structure of the interferograms was demonstrated even when the magnetic field becomes large enough to refocus the electron trajectories. Constancy of the internal phase was quantitatively confirmed by the comparison of electron affinity measurements made with and without such magnetic fields. As a consequence, the uncertainty of some previous eA measurements appears to have been overestimated, which leads to a revision of the electron affinities of oxygen, silicon and sulfur. Investigation of higher field regimes where the cyclotron period would become of the same order of magnitude or larger than the inverse of the time-of-flight difference of the interfering trajectories is left to future studies.

The authors acknowledge the assistance of Fabienne Goldfarb and Simon Canlet for their calculations and tests, respectively, during the construction of the two crossed pairs of magnetic-field rectangular coils. They are also grateful to Mickaël Vandevraye for some useful comments. This work was supported by the Agence nationale de la recherche under contract ANR-06-BLAN-0012-01.

Appendix: Closed-orbit perturbative calculation of the interference phase at the centre of the ring pattern in the presence of a weak magnetic field

A.1 The role of a closed classical orbit

In a semi-classical analysis, the phase difference in the interferogram is just \hbar^{-1} times (with \hbar the reduced Planck constant) the reduced action difference between the two trajectories that lead to the detection point. The maximum phase difference $\Delta\phi$, which is reached at the centre of our ring pattern in the absence of any deviation from the circular symmetry, will thus correspond to a maximum action difference. Since the action gradient in the detection plane is just the final momentum \mathbf{p} , any extremum of the action difference corresponds to the identity of the final momenta. The final parts of the interfering trajectories are thus necessarily superposed, so the only possibility apart from the trivial degenerate case is that the longer trajectory makes a loop before merging with the shorter one. All the extreme action difference is thus built in a closed loop that brings the electron back to the origin.

The further importance of underlying closed classical orbits for the spectral properties of the photoionization or photodetachment cross-sections was demonstrated by Du and Delos [30,31] for photoionization in a magnetic field, then developed for photodetachment in external fields [16, 32]. In the spatial domain however, as just seen, the role of closed loops directly stems from the identification of the action gradient with the momentum.

On the other hand, the reduced action’s partial derivative with respect to energy ε is just the time-of-flight T . So the reduced action difference can be calculated as an antiderivative of the time difference ΔT , i.e. here the time taken by the closed loop. As a consequence

$$\Delta\phi = \frac{1}{\hbar} \int_0^\varepsilon \Delta T(\varepsilon') d\varepsilon'. \quad (\text{A.1})$$

The aim of the present appendix is to calculate this phase difference in the presence of both an electric and a magnetic field, so as to determine from a perturbative point of view the phase variations produced in photodetachment microscopy interferograms by the addition of a weak magnetic field.

A.2 Notations and initial conditions

We define a Cartesian reference frame $Oxyz$ of electron coordinates (x, y, z) so as to write the electric and magnetic fields $\mathbf{E} = (0, 0, -E)$ and $\mathbf{B} = (B_x, 0, B_z)$ respectively, with $E > 0$ (which will make the electron ‘fall’ to positive z values) and the origin O set at the position of the negative ion (which is the electron source). We note $B = |\mathbf{B}|$. We define the electron acceleration $\boldsymbol{\gamma} = q\mathbf{E}/m$ $\boldsymbol{\Omega} = q\mathbf{B}/m$, where $q = -e$ and m are respectively the charge and the mass of the electron; their components

are given by $\boldsymbol{\gamma} = (0, 0, \gamma)$ and $\boldsymbol{\Omega} = (\Omega_x, 0, \Omega_z)$, where $\gamma = eE/m$, $\Omega_x = -eB_x/m$, $\Omega_z = -eB_z/m$ can be algebraic quantities. $\Omega = |\boldsymbol{\Omega}| = (\Omega_x^2 + \Omega_z^2)^{1/2} = eB/m$ is the cyclotron angular frequency, equal to twice the Larmor frequency. Reduced dimensionless cyclotron frequencies can be defined by $\omega_x = \Omega_x/\Omega = -B_x/B$ and $\omega_z = \Omega_z/\Omega = -B_z/B$.

At time t , the velocity of the electron is $\mathbf{V} = (\dot{x}, \dot{y}, \dot{z})$. At time $t = 0$ and at the origin O, the initial velocity of the electron $\mathbf{V}_0 = (V_{0x}, V_{0y}, V_{0z})$ is such that $V_0 = |\mathbf{V}_0| = (2\varepsilon/m)^{1/2}$, where ε is the initial kinetic energy of the photodetached electron. The experimental orders of magnitude are: $V_0 \sim 10^3\text{--}10^4$ m/s, $E \sim 300$ V/m, $B \sim 10^{-5}\text{--}10^{-4}$ T so $\eta \equiv V_0 B/E \sim 10^{-4}\text{--}10^{-3}$.

A.3 Newton's second law and the equations of motion of the electron

The maximum electron speed being typically 10^7 m/s, non relativistic Newton's second law can be applied to the electron subject to the Lorentz force: $m\boldsymbol{\gamma} = -e(\mathbf{E} + \mathbf{V} \wedge \mathbf{B})$. With the notations of Section 2, one can write the resulting system of coupled, linear differential equations:

$$\ddot{x} = \Omega_z \dot{y}; \quad \ddot{y} = \Omega_x \dot{z} - \Omega_z \dot{x}; \quad \ddot{z} = \gamma - \Omega_x \dot{y}.$$

Solving such a system of differential equations is straightforward. The motion equations of the electron can be written in the following form:

$$x(t) = \Omega^{-2} [a\Omega_z(1 - \cos \Omega t) - b\Omega_z \sin \Omega t + (1/2)\Omega_x\Omega_z\gamma t^2 + c\Omega_x\Omega^2 t] \quad (\text{A.2a})$$

$$y(t) = \Omega^{-2} [a\Omega \sin \Omega t + b\Omega(1 - \cos \Omega t) + \Omega_x\gamma t] \quad (\text{A.2b})$$

$$z(t) = \Omega^{-2} [-a\Omega_x(1 - \cos \Omega t) + b\Omega_x \sin \Omega t + (1/2)\Omega_z^2\gamma t^2 + c\Omega_z\Omega^2 t] \quad (\text{A.2c})$$

where the constants a , b , c are defined from the initial conditions:

$$a = V_{0y} - \Omega_x\Omega^{-2}\gamma; \quad b = \Omega^{-1}[\Omega_x V_{0z} - \Omega_z V_{0x}]; \\ c = \Omega^{-2}[\Omega_x V_{0x} + \Omega_z V_{0z}]. \quad (\text{A.3})$$

A.4 Equations for closed orbits

Spherical polar coordinates (r, θ, φ) can be used to characterize the emission vector of the photoelectron. The Cartesian components of \mathbf{V}_0 will be:

$$V_{0x} = V_0 \sin \theta \cos \varphi, \quad V_{0y} = V_0 \sin \theta \sin \varphi, \\ V_{0z} = V_0 \cos \theta.$$

A closed orbit is defined by the conditions on the expressions (A.2):

$$x(\Delta T) = 0, \quad y(\Delta T) = 0, \quad z(\Delta T) = 0 \quad (\text{A.4})$$

which has to be resolved to determine the initial velocity of a closed loop. In the absence of magnetic field ($B = 0$,

$\Omega = 0$), the only possible closed orbit is the up and down round trip along the axis Oz, which is defined by $\theta = \pi$ and any value of φ . The determination of the revolution time is straightforward:

$$\Delta T_0(\varepsilon) = 2 \frac{V_0}{\gamma} = 2 \frac{\sqrt{2m}}{eE} \varepsilon^{1/2}. \quad (\text{A.5})$$

The phase difference on the Oz axis, obtained from integration (A1), is just the maximum phase $\Delta\phi_0$ at the centre of the ring patterns in photodetachment microscopy [33]:

$$\Delta\phi_0 = \frac{4\sqrt{2m}}{3\hbar eE} \varepsilon^{3/2}. \quad (\text{A.6})$$

In the general case, i.e. with a non-zero B_x component, expressing the condition that a closed loop shall bring the electron back to the origin with the same kinetic energy, one easily finds that an orbit can be closed only if $V_{0x} = 0$, i.e. $\varphi = \pi/2$ ($\Omega_x > 0$, $B_x < 0$) or $\varphi = -\pi/2$ ($\Omega_x < 0$, $B_x > 0$). The inclination θ can be developed in the vicinity of $\theta = \pi$ as a power series of η . Up to the fifth order in η the closed-orbit time-of-flight appears to be:

$$\Delta T = \frac{k}{\Omega} = \Delta T_0 \left[1 - \frac{1}{18} \omega_x^2 \eta^2 + \left(\frac{7}{648} \omega_x^2 - \frac{1}{135} \right) \omega_x^2 \eta^4 \right] \quad (\text{A.7})$$

$$\Delta T(\varepsilon) = \Delta T_0(\varepsilon) \left[1 - \frac{1}{9} \frac{B_x^2}{mE^2} \varepsilon + \left(\frac{7}{162} - \frac{4}{135} \frac{B^2}{B_x^2} \right) \frac{B_x^4}{m^2 E^4} \varepsilon^2 \right]. \quad (\text{A.8})$$

The integration (A.1) of (A.8), determines the variation of the maximum phase $\Delta\phi$ at the centre of the interferograms with respect to $\Delta\phi_0$ (A6):

$$\Delta\phi = \Delta\phi_0 \left[1 - \frac{1}{15} \frac{B_x^2}{mE^2} \varepsilon + \left(\frac{1}{54} - \frac{4}{315} \frac{B^2}{B_x^2} \right) \frac{B_x^4}{m^2 E^4} \varepsilon^2 \right]. \quad (\text{A.9})$$

In the expression (A.9), the second term is independent of B_z , but not the third term. With the typical values of Section 2, the second and third terms of the parenthesis are respectively lower than 10^{-9} and 10^{-17} . This result shows that, in the present experimental conditions of photodetachment microscopy, the influence of the magnetic field on the interferograms, even with an arbitrary orientation, remains completely negligible.

References

1. Yu.N. Demkov, V.D. Kondratovich, V.N. Ostrovskii, Pis'ma Zh. Eksp. Teor. Fiz. **34**, 425 (1981) [JETP Lett. **34**, 403 (1981)]
2. C. Blondel, C. Delsart, F. Dulieu, Phys. Rev. Lett. **77**, 3755 (1996)
3. C. Blondel, C. Delsart, F. Dulieu, C. Valli, Eur. Phys. J. D **5**, 207 (1999)
4. C. Blondel, W. Chaibi, C. Delsart, C. Drag, F. Goldfarb, S. Kröger, Eur. Phys. J. D **33**, 335 (2005)
5. W. Chaibi, C. Delsart, C. Drag, C. Blondel, J. Mol. Spectrosc. **239**, 11 (2006)

6. W. Chaibi, C. Blondel, C. Delsart, C. Drag, *Europhys. Lett.* **82**, 20005 (2008)
7. C. Bracher, T. Kramer, J.B. Delos, *Phys. Rev. A* **73**, 062114 (2006), and references therein
8. C. Bracher, J.B. Delos, *Phys. Rev. Lett.* **96**, 100404 (2006)
9. S. Gao, G.C. Yang, S.L. Lin, M.L. Du, *Eur. Phys. J. D* **42**, 189 (2007)
10. M.L. Du, *Phys. Rev. A* **70**, 055402 (2004), and references therein
11. A.K. Langworthy, D.M. Pendergrast, J.N. Yukich, *Phys. Rev. A* **69**, 025401 (2004), and references therein
12. J.D. Rudmin, L.P. Ratliff, J.N. Yukich, D.J. Larson, *J. Phys. B* **29**, L881 (1996)
13. I.I. Fabrikant, *Phys. Rev. A* **43**, 258 (1991)
14. A.D. Peters, C. Jaffé, J.B. Delos, *Phys. Rev. A* **56**, 331 (1997), and references therein
15. A.D. Peters, C. Jaffé, J. Gao, J.B. Delos, *Phys. Rev. A* **56**, 345 (1997)
16. A.D. Peters, J.B. Delos, *Phys. Rev. A* **47**, 3020 (1993)
17. Z.Y. Liu, D.H. Wang, *Phys. Rev. A* **55**, 4605 (1997)
18. Z.Y. Liu, D.H. Wang, *Phys. Rev. A* **56**, 2670 (1997)
19. W. De-Hua, D. Shi-Liang, *Chin. Phys.* **16**, 0671 (2007)
20. J.N. Yukich, T. Kramer, C. Bracher, *Phys. Rev. A* **68**, 033412 (2003)
21. T. Kramer, C. Bracher, M. Kleber, *J. Opt. B: Quantum Semiclass. Opt.* **6**, 21 (2004), and references therein
22. C. Blondel, W. Chaibi, C. Delsart, C. Drag, *J. Phys. B* **39**, 1409 (2006)
23. C. Blondel, C. Delsart, F. Goldfarb, *J. Phys. B* **34**, L281 (2001)
24. C. Blondel, C. Delsart, F. Goldfarb, *J. Phys. B* **34**, 2757 (2001)
25. T. Kramer, C. Bracher, M. Kleber, *Europhys. Lett.* **56**, 471 (2001)
26. C. Blondel, S. Berge, C. Delsart, *Am. J. Phys.* **69**, 810 (2001)
27. W.A.M. Blumberg, W.M. Itano, D.J. Larson, *Phys. Rev. A* **19**, 139 (1979)
28. P.J. Mohr, B.N. Taylor, D.B. Newell, *Rev. Mod. Phys.* **80**, 633 (2008), <http://physics.nist.gov/cuu/Constants/index.html>
29. T. Carette, C. Drag, O. Scharf, C. Blondel, C. Delsart, C. Froese-Fischer, M. Godefroid, *Phys. Rev. A* (in press)
30. M.L. Du, J.B. Delos, *Phys. Rev. Lett.* **58**, 1731 (1987)
31. M.L. Du, J.B. Delos, *Phys. Rev. A* **38**, 1896 (1988)
32. M.L. Du, J.B. Delos, *Phys. Rev. A* **38**, 5609 (1988)
33. C. Valli, C. Blondel, C. Delsart, *Phys. Rev. A* **59**, 3809 (1999)